Horizontal thermocapillary convection of succinonitrile: Steady state, instabilities, and transition to chaos

Edoardo Bucchignani*

Centro Italiano Ricerche Aerospariali, Via Maiorise, 81043 Capua (CE), Italy

Daniela Mansutti†

Istituto per le Applicazioni del Calcolo (C.N.R.), Viale del Policlinico 137, 00161 Roma, Italy

We present the bifurcation pattern of the thermocapillary horizontal convection flow of succinonitrile (SCN) in an open top parallelepipedic cavity with dimensions $4 \times 1 \times 1$. The bifurcation parameter is the Rayleigh number (Ra) that was investigated in the range $[150; 5 \times 10^8]$ while the Marangoni number (Ma) was kept at Ma$=10^4$. Several steady flow configurations are described for Ra$\leq 5 \times 10^7$. Then the occurrence of periodic and quasiperiodic flows is shown for values of Ra$< 5 \times 10^8$ and at Ra$=5 \times 10^8$ the chaos arises. It is also proved numerically the coexistence of different temporal regimes at the same value of Ra according to the thermal history of the fluid.

I. INTRODUCTION

During the growth of metal and semiconductor crystals from a liquid melt in a horizontal boat, undesirable striations corresponding to an irregular distribution of solute substances in the crystal may occur. It has been shown that such striations are caused by spontaneous temperature oscillations generating fluctuations in the rate of growth of the crystal [1]. Experiments without solidifications carried out for pure molten gallium [2] with a horizontal temperature gradient exhibit such oscillations. It has been found that for small temperature differences ΔT, the flow is steady and simply unicellular (so-called *return flow*). While for ΔT larger than a critical value, the fluid flow reaches an oscillatory regime.

A large amount of research has been done on the model of the float-zone crystal-growth process (known as the *half-zone*). In this model, a liquid bridge is held in place by surface tension forces between two coaxial cylindrical rods at different temperatures. The first results about oscillatory convection in half-zones are from the work of Schwabe *et al.* [3]. Moreover, the transition from steady to oscillatory thermocapillary convection has been studied theoretically by many authors, in different geometries. Several distinct instability mechanisms leading to oscillatory flow have been demonstrated. Smith and Davis [4] discovered the *return flow* instability called hydrothermal waves, which is a temperature disturbance wave that propagates in a direction that depends on the Prandtl number (Pr). For example, when the Prandtl number is small and the inertial forces are dominating, it was seen that it propagates spanwise (perpendicular to the surface flow); on the contrary, for large Prandtl numbers, it propagates along the upstream direction. They also found the surface wave instability, which is caused by the interaction of the base state shear at the open top and the velocity

disturbance induced by a perturbation of the free surface. Experiments have been conducted by Riley and Neitzel [5] to investigate the hydrothermal-wave instability in a cavity filled with a silicon oil (Pr$=14$). The transition from a steady unicellular flow to hydrothermal wave was observed in a thin layer ($H/L=1/30$) while experiments in a deep layer do not show this kind of instability, but rather a transition to steady multicellular structure and then to oscillatory flow.

In two-dimensional containers, Villers and Platten [6] observed a steady roll structure that becomes oscillatory when the thermal forcing is increased. It may be related to the instability mechanism investigated by Smith [7] in the case of a large Prandtl number. For small Prandtl numbers, the instabilities seems to be entirely of hydrodynamical kind, as shown by Ben Hadid and Roux [8] who found temperature and velocity fields totally decoupled in their simulations.

Although the study of flows driven by the combined action of buoyancy and thermocapillary forces has been the subject of intense investigations (both numerically and experimentally) there is still a lack of knowledge about the transition to chaos. In the present work we describe our investigation on this aspect. We have studied numerically the flows of pure succinonitrile (SCN) (Pr$=23$) developing in a parallelepipedic cavity ($4 \times 1 \times 1$). This choice is due to the fact that during solidification processes this material behaves like a metal but it is transparent and hence is suitable for validations by physical experiments. In our tests the Marangoni number has been kept constantly Ma$=10^4$, while the Rayleigh number has been increased up to 5×10^8 in order to analyze the transition mechanism to the chaos. Even if a precise scientific definition of chaos does not exist, our common experience is related to some of its typical properties, the most representative of which is the (partial) *unpredictability of the results:* A chaotic system loses the memory of itself or, in other words, the knowledge of the status of the system for a finite time interval does not allow us to foresee its further evolution. In the last 20 years, three main scenarios that lead to chaos have been classified and deeply

*Electronic address: e.bucchignani@cira.it

†Electronic address: mansutti@iac.rm.cnr.it
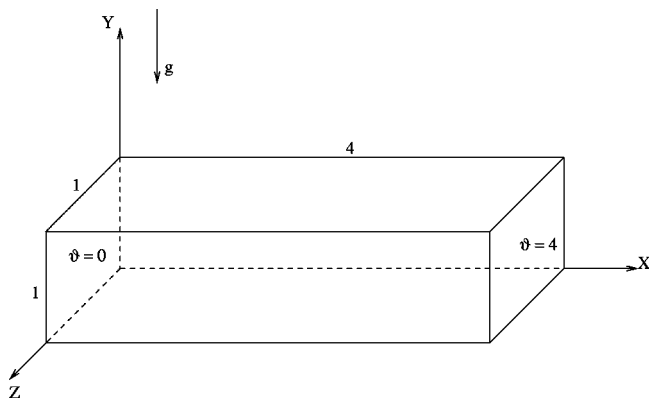
FIG. 1. The computational domain.

investigated according to the different sequence of temporal regimes: the Feigenbaum cascade, the Ruelle-Takens route, and the Manneville-Pomeau route [10]. These transition paths have been detected in several systems, both numerically and experimentally [11–14]. In our case we have obtained the numerical evidence that the system evolves to chaos following the Ruelle-Takens route, that is passing through the following flow regimes, steady, periodic, quasiperiodic with two frequencies, and quasiperiodic with three frequencies. Besides, it should be noted that another bifurcation branch has been detected through just steady flow regimes. The presence of multiple stable flows qualifies the system as strongly dependent on its thermal history.

The numerical simulations described here are obtained by a finite discretization of the vorticity-velocity formulation of the Navier-Stokes equations for incompressible nonisothermal fluids. The discrete model is solved by a true transient procedure that guarantees the fulfillment of the mass conservation law and of the vorticity definition up to round-off error.

This paper is structured as follows: In the next two paragraphs, the mathematical formulation and the solution procedure are briefly explained, respectively, then the presentation and discussion of the numerical results follow.

II. FORMULATION OF THE PROBLEM

The flow domain considered here is a parallelepipedic cavity whose dimensions are $L_x=4$, $L_z=1$, and $H=1$ (H is the vertical dimension) (Fig. 1). Within a counter-rotating reference frame, the y direction is the vertical one. This cavity is filled with SCN. A driving temperature difference in the x direction is imposed by properly prescribing the temperature at the two vertical solid walls at $x=0$ and $x=L_x$; the four remaining boundaries are assumed to be insulated and require adiabatic boundary conditions. The top free surface, located at $y=H$, is supposed to be flat; the gas above the free surface is assumed to have negligible viscosity and conductivity so that it does not influence the flow and temperature fields of SCN. For the liquid of interest, surface tension decreases with increasing temperature and the following linear function is considered an adequate approximation to this relation:

$$\sigma = \sigma_r - \gamma(\theta - \theta_r),$$

$$\gamma = \frac{\partial \sigma}{\partial \theta}.$$

Through the tangential stress balance at the interface, surface gradients of the temperature field generate an interfacial shear stress which drives the surface flow in the direction opposite to that of the temperature gradient (see Sec. II A).

The SCN flow is governed by the Navier-Stokes equations and the Boussinesq approximation is assumed to hold. The formulation in terms of vorticity $\boldsymbol{\omega}$, velocity $u = (u, v, w)$, and temperature θ follows:

$$\frac{\partial \boldsymbol{\omega}}{\partial t} + \boldsymbol{\nabla} \times (\boldsymbol{\omega} \times \mathbf{u}) = \frac{\mathrm{Pr}}{\mathrm{Ma}} \nabla^2 \boldsymbol{\omega} - \frac{\mathrm{Ra}\,\mathrm{Pr}}{\mathrm{Ma}^2} \boldsymbol{\nabla} \times \left(\theta \frac{\mathbf{g}}{|g|} \right),$$

$$(1)$$

$$\nabla^2 \mathbf{u} = - \boldsymbol{\nabla} \times \boldsymbol{\omega},$$ (2)

$$\frac{\partial \theta}{\partial t} + (\mathbf{u} \cdot \boldsymbol{\nabla}) \theta = \frac{1}{Ma} \nabla^2 \theta.$$ (3)

We remind the reader that the nondimensional parameters Ra, Pr and Ma are defined as

$$\mathrm{Ra} = \frac{g\beta\Delta T H^3}{\kappa\nu}, \quad \mathrm{Pr} = \frac{\nu}{\kappa}, \quad \mathrm{Ma} = \frac{\gamma\Delta T H}{\mu\kappa},$$

where, beside the known quantities, g is the gravitational acceleration, β is the coefficient of thermal expansion, ΔT is the temperature difference between the opposite vertical walls, κ is the thermal diffusivity, ν is the kinematic viscosity, and μ is the dynamic viscosity. The non-dimensional scheme adopted is based on the reference velocity $u^*=\gamma\Delta T/\mu$ and the reference time $t^*=H\mu/\gamma\Delta T$. This scheme is particularly advantageous, as it avoids the presence of non-dimensional parameters in the expression of the boundary condition at the free surface.

During the simulations, the heat flux from the hot to cold wall through a section S has been evaluated by means of the mean Nusselt number

$$\mathrm{Nu} = \frac{1}{S} \int_S (\theta\mathbf{u} - \boldsymbol{\nabla}\,\theta) \cdot \mathbf{n} dS.$$

This expression represents the ratio between the total heat flux versus the heat flux related to the purely diffusive case.

A. Boundary conditions

The above formulation allows a very simple form of the boundary conditions

(1) The boundary conditions associated with Eq. (1) are obtained by the vorticity definition written on the boundary. We shall see in the following paragraph that the time discretization scheme used handles this boundary condition by updating vorticity and enforcing its definition at each time step. This procedure contributes to the correct coupling between the kinematic and the dynamic parts of the problem.

TABLE I. Mesh sensitivity analysis: Pr=23, Ra=1000, Ma = 10 000.

	$25 \times 15 \times 15$	$41 \times 21 \times 21$	$61 \times 31 \times 31$
u_{max}	5.523×10^{-2}	5.666×10^{-2}	5.737×10^{-2}
v_{max}	2.854×10^{-2}	2.767×10^{-2}	2.723×10^{-2}
w_{max}	0.798×10^{-2}	0.791×10^{-2}	0.788×10^{-2}
Nu	14.824	15.973	16.548

TABLE II. Thermophysical properties of pure SCN.

Property	Value
Melting point	$T_m = 54\ °C$
Density	$\rho = 988\ Kg/m^3$
Thermal expansion	$\beta = 7 \times 10^{-4}\ K^{-1}$
Viscosity	$\mu = 2.56 \times 10^{-3} Kg/ms$
Kinematic viscosity	$\nu = 2.591 \times 10^{-6} m^2/s$
Thermal conductivity	$\lambda = 0.223\ W/mK$
Thermal diffusivity	$\kappa = 1.127 \times 10^{-7} m^2/s$
Prandtl number	Pr=23

(2) Dirichlet boundary conditions are associated to the elliptic velocity Eq. (2). In particular null velocity field is assigned at the solid walls; at the top free surface it holds

$$v = 0,$$

$$\frac{\partial u}{\partial y} = -\frac{\partial \theta}{\partial x},$$

$$\frac{\partial w}{\partial y} = -\frac{\partial \theta}{\partial z},$$

where the last two conditions are obtained by enforcing the second dynamics law. We observe that the second condition above introduces a jump discontinuity at $x=0$ and $x=4$. Actually at those cartesian planes the velocity component u is null due to the presence of a rigid wall; consequently, $\partial u/\partial y$ is null. On the contrary, at the free surface, $\partial \theta/\partial x$ is a measure of the thermocapillary effects and is not at all vanishing. However this inconsistency of the formulation has no effect within the numerical solution procedure here adopted because this is based on a finite difference discretization and the discontinuity edge is left out of the computational domain as if regularized boundary values were imposed.

(3) The boundary conditions for the energy equation are easily derived from the definitions and are of Dirichlet or Neumann type in those portions of the boundary where, respectively, the value of temperature or its normal derivative are known.

$$\theta = T_c \text{ at } x = 0,$$

$$\theta = T_h \text{ at } x = L_x,$$

$$\frac{\partial \theta}{\partial n} = 0 \text{ at } \begin{cases} y = 0, y = H, \\ z = 0, z = L_z. \end{cases}$$

The hypothesis, here assumed, that the top free surface of the cavity is flat is consistent with the presence of an oil film that counteracts the effects of the surface tension gradients in the vertical direction (y) eventually enhanced by heat flux in the same direction. On the other hand, as it was just illustrated, in the present case, heat flux at the top free surface is assumed to be null.

III. NUMERICAL METHOD

The governing Eqs. (1)–(3) together with the proper boundary conditions are discretized by using finite difference approximations. Spatial derivatives are discretized on a uniform mesh through central second-order differences while time derivatives are discretized through a three-point second-order backward differences. Maximum accuracy is allowed by a staggered variable location. At this purpose the MAC (Marker and Cell) stencil, originally built for the $(\mathbf{u}, \theta)$ formulation by Harlow and Welch [15], has been adapted to the present $(\mathbf{u}, \boldsymbol{\omega}, \theta)$ formulation. In general when each velocity component is evaluated at the center of the faces of the computational cells, which are orthogonal, the mass conservation law at the discrete level can be satisfied up to a round-off error. In a similar way, by evaluating the vorticity components at the mid-point of the edges of the computational cell which are parallel, the natural property of solenoidality of the vorticity can be met at the discrete level up to a round-off error. Furthermore in our model, staggering of the variables allows us to discretize Eq. (2) without any need of variable averaging. However in discretizing Eq. (1) averaging is still necessary for the treatment of the advective term $\nabla \times (\boldsymbol{\omega} \times \mathbf{u})$, where the product $\boldsymbol{\omega} \times \mathbf{u}$ is here averaged in the whole. In this way the resulting discrete equation is consistent with the implicit property of solenoidality of the vorticity field expressed in discrete form.

The computation of the numerical solutions has been performed by a time dependent algorithm. A true transient procedure requires particular care when used together with the vorticity-velocity formulation. In fact the continuity equation is imposed only in an implicit way by dropping the term $\nabla \times \mathbf{u}$ in Eqs. (1)–(3) so that mass conservation and definition of vorticity could be violated if strong coupling of the full set of the equations is not ensured. The time integration has been developed by means of an implicit numerical scheme that has been linearized through the "frozen coefficients" technique [16].

In this way at each time step our original system of partial differential equations gives rise to a large linear system of equations of the type

$$\mathbf{A}x = b,$$

where x is the unknown vector and b is the known vector. The coefficient matrix $\mathbf{A}$ has a very sparse structure. The solution of this linear system via a direct method is obviously not recommended due to the size of the problem, and an iterative procedure has been adopted, a variant of precon-

TABLE III. Value of Ra, corresponding maximum values of velocity components, Nusselt number in the middle plane normal to the x axis and temporal regime.

Ra	u_{max}	v_{max}	w_{max}	Nu_x	Regime
1.5×10^2	4.925×10^{-2}	2.422×10^{-2}	0.708×10^{-2}	15.741	S
10^3	5.666×10^{-2}	2.767×10^{-2}	0.791×10^{-2}	15.973	S
10^4	4.728×10^{-2}	2.433×10^{-2}	0.719×10^{-2}	18.640	S
10^5	3.671×10^{-2}	2.527×10^{-2}	0.925×10^{-2}	27.539	S
10^6	4.392×10^{-2}	4.418×10^{-2}	1.001×10^{-2}	36.251	S
5×10^6	5.835×10^{-2}	5.293×10^{-2}	1.310×10^{-2}	39.431	S
10^7	7.414×10^{-2}	6.383×10^{-2}	1.751×10^{-2}	44.490	S
5×10^7	0.107	7.439×10^{-2}	2.766×10^{-2}	49.638	S

ditioned conjugate gradient. This approach has the advantage to allow a great flexibility in writing the discretized form of numerical model. We have used the Bi-CGSTAB (biconjugate gradient stabilized) algorithm [16,17], because of its numerical stability and speed of convergence.

Although, from a theoretical point of view, iterative methods can be used without preconditioning the linear systems of equations, the use of a preconditioning technique is, in many practical applications, essential to fulfil the convergence and stability requirements of the iterative procedure itself. The aim of the preconditioner is to convert the original linear system to an equivalent but better-conditioned system. This consists of finding a real matrix C such that the new linear system

$$C^{-1}\mathbf{A}x = C^{-1}b$$

has (by construction) better convergence and stability characteristics than the original system. It is obvious that the matrix C must be chosen carefully so that C^{-1} should be close to the inverse of $\mathbf{A}$ and easy to be inverted in order to compress the computational cost. As a matter of fact the ILU (incomplete LU) factorization is one of the most robust and widely used preconditioners: C is defined as the product LU of a lower (L) and an upper (U) triangular matrix generated by a variant of the Crout factorization algorithm where only the elements of $\mathbf{A}$ that are originally nonzero are factorized and stored. In this way the sparsity structure of $\mathbf{A}$ is completely preserved. Testing of the described numerical model has been extensively discussed in Ref. [16].

The numerical inaccuracies reported here in meeting mass conservation and vorticity definition had the same order of magnitude as the round-off error at each time step. The criterion used in order to assess the steadiness of the flow is based on the numerical evaluation of the time derivative of ω averaged on the whole flow field, when this value is

(a)

(b)

(c)

(d)
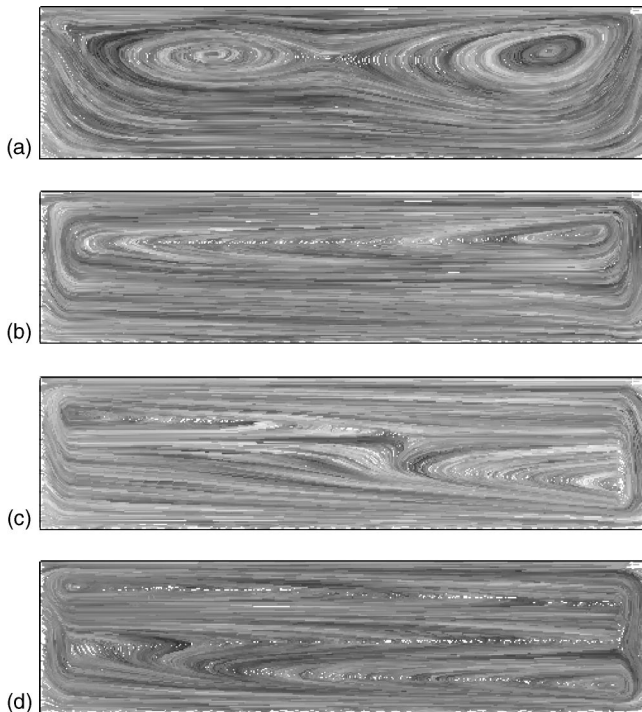
FIG. 2. Pr=23, Ma=10 000—LIC representation at the plane $z=0.5$ at Ra=150 (a), 10^5 (b), 5×10^6 (c), and 5×10^7 (d).

(a)

(b)

(c)

(d)
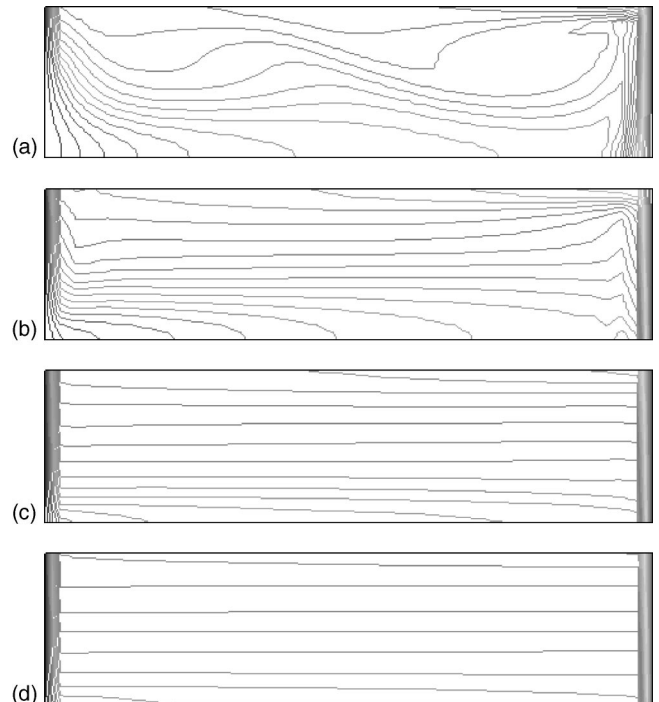
FIG. 3. Pr=23, Ma=10 000—Isothermal lines at the plane $z=0.5$ at Ra=150 (a), 10^5 (b), 5×10^6 (c), and 5×10^7 (d).

TABLE IV. Transition to the chaos: List of temporal regimes obtained as a function of the increase in Ra.

From Ra		To Ra	Regime
5×10^7	$\rightarrow$	10^8	S
5×10^7	$\rightarrow$	4.25×10^8	P
5×10^7	$\rightarrow$	4.3×10^8	QP_2
5×10^7	$\rightarrow$	4.5×10^8	QP_2
5×10^7	$\rightarrow$	5×10^8	N

smaller than a fixed quantity (10^{-9}) the flow is considered steady.

The visualization of the numerical flows has been realized by means of LIC (line integral convolution), which is a vector field representation for the global realistic visualization of a surface flow [18]. In contrast to tracing single streamlines, the LIC technique is based on the tracing of a high number of relatively short streamlines, that are actually convoluted with an initially random distribution of black and white points on the target surface (seeds). Resulting LIC images appear very similar to some typical flow visualizations (oil flow patterns), thus well suited for numerical-experimental comparison. However, it is worth observing that LIC allows only qualitative comparisons, therefore numerical tables are also included.

IV. RESULTS

The numerical model described above was adopted to solve several thermal convection flow problems in parallel-epipedic domains and the computational code was repeatedly validated as mentioned in Ref. [14]. In the study of the horizontal thermal convection flow in a shallow three-dimensional closed cavity, the space mesh sensitivity analysis lead the authors to the conclusion that a mesh with a spatial resolution of 0.05 in the vertical direction is sufficient to obtain accurate results [14]. Due to the physical similarities of the present flow problem, we expect that the same spatial resolution (corresponding on the chosen domain to a $41 \times 21 \times 21$ space grid) is sufficient to describe the whole flow structures. Anyway a space mesh refinement analysis has been developed for the case at Ra=1000 and Ma =10 000. The list of the values of u_{max}, v_{max}, w_{max}, and Nu_x, respectively, the maximum of the modulus of each velocity component, and the Nusselt number at the middle plane nor-

TABLE V. Value of Ra, corresponding maximum values of velocity components, Nusselt number in the middle plane normal to the x axis and temporal regime.

Ra	u_{max}	v_{max}	w_{max}	Nu_x	Regime
4.25×10^8	0.142	0.097	0.377×10^{-1}	61.628	P
4.3×10^8	0.179	0.170	0.589×10^{-1}	68.854	QP_2
4.5×10^8	0.313	0.880	0.211	95.523	QP_2
5×10^8	0.453	1.192	0.284	52.683	N
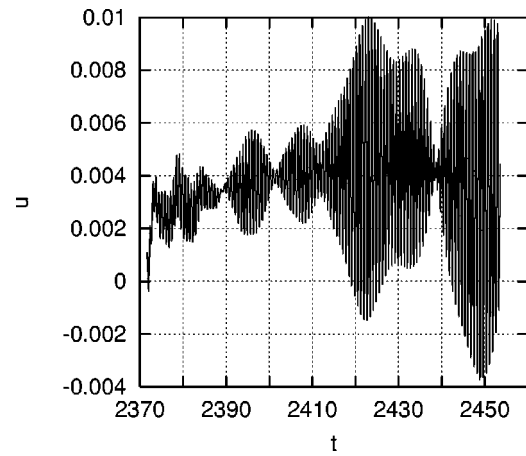
FIG. 4. Pr=23, Ra=4.3×10^8, and Ma=10 000—Time history of the x component of velocity (u) at the point (0.8, 0.5, 0.4).

mal to the x axis, obtained at different space meshes, is displayed in Table I.

A rapid inspection confirms the adequacy of the average grid that is used in the numerical tests of the following paragraphs. It is worth mentioning that by time and space mesh sensitivity analysis in a two-dimensional problem we reached the conclusion that the numerical model is "nearly" second order accurate both in time and in space as reported in Ref. [16]. Actually the linearization procedure applied to the convective terms within the discretized equations slightly lowers the degree of accuracy of the overall discrete operator with respect to the single discrete schemes used.

In Table II, we recall the thermophysical properties of pure SCN (Pr=23), the transparent organic plastic fluid that fills the cavity.

The nondimensional values of temperature at cold and hot walls are, respectively, $T_c=0$ and $T_h=4$. A series of numerical simulations has been performed assuming that the Marangoni number is constant and equal to 10 000, while the Rayleigh number has been changed in a wide range, from 150 to 5×10^8, in order to understand the influence of the increasing buoyancy on the physical mechanism of the flow instability. Instabilities of both types, spatial and temporal,
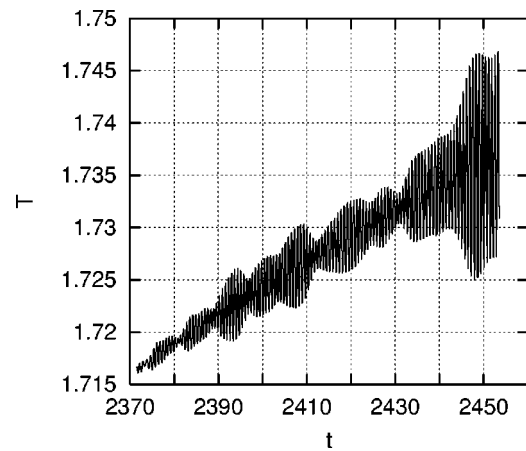
FIG. 5. Pr=23, Ra=4.3×10^8, and Ma=10 000—Time history of the temperature at the point (0.8, 0.5, 0.4).
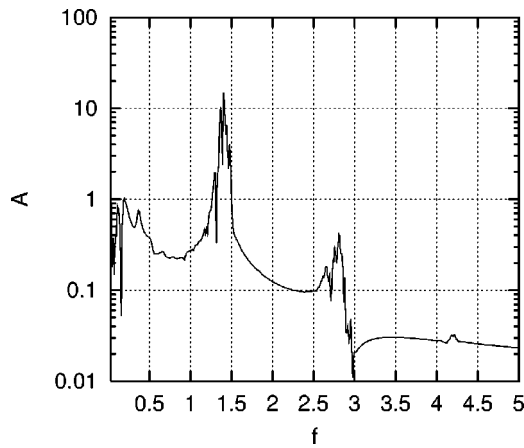
FIG. 6. Pr=23, Ra=4.3×10^8, and Ma=10 000—FFT applied on the time history of the x component of velocity (u) at the point (0.8, 0.5, 0.4).

have been detected. The following nomenclature has been adopted in order to characterize the occurring temporal regimes:

(a) *S*. steady state;

(b) *P*. periodic regime with one fundamental frequency;

(c) QP_2. quasiperiodic regime with two incommensurate frequencies;

(d) QP_3. quasiperiodic regime with three incommensurate frequencies;

(e) *N*. chaotic regime.

The parallel flow solution valid for an infinite layer yields a simple cubic polynomial expression for the horizontal velocity profile $u(y)$, taking into account both the thermocapillary and the buoyancy effects, while a simpler parabolic profile is obtained when thermocapillarity acts alone. Such explicit forms are very useful to adopt when one is interested in the basic convective states, for low values of the control parameters; however, for limited domains they are valid only in the core region; besides, for increasing values of the control parameters the basic flow is more and more distorted and finally undergoes a transition to unsteady regimes as it will be shown in the next paragraphs.

A basic finding of our investigation is that each spatial/temporal instability which characterizes the system for an assigned Ra is not uniquely determined but it depends on the chosen growth rate of Ra between subsequent simulations, or, in other words, it depends on the thermal history of the flow.
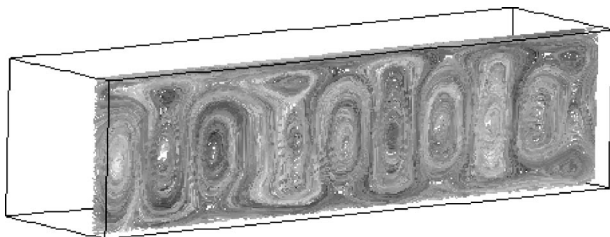
FIG. 7. Pr=23, Ra=4.3×10^8, and Ma=10 000—LIC representation at the plane $z=0.15$.
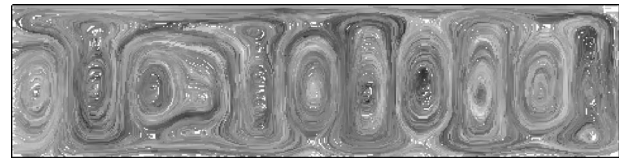
FIG. 8. Pr=23, Ra=4.3×10^8, and Ma=10 000—LIC representation at the plane $z=0.5$.

A. Steady flow configurations

The first simulation has been conducted assuming the value Ra=150 and starting from rest. Further simulations have been executed for increasing values of Ra, starting from the flow, and thermal fields obtained at the last considered value of Ra. For values of Ra up to 5×10^7 steady solutions were obtained. Table III reports the maximum values of the three velocity components and the average Nusselt number in the x direction as a function of Ra. In Fig. 2 the flow configuration at four selected values of Ra can be seen. In this figure, the LIC representations in the z-normal plane at $z=0.5$ are shown. The corresponding isothermal lines in the same section are shown in Fig. 3.

At Ra=150, a large counterclockwise circulation pushed toward the hot wall is apparent. This is typical of fluids having Pr larger than 10. Besides, a second smaller vortex appears, localized at about $x=1.5$. There is no significant difference among the z-normal planes so that the flow appears two-dimensional. The temperature variation from the cold to hot wall is not monotonic, due to the contribution of the thermocapillary effects. Temperature gradients are largest near the hot and cold walls, while the gradient near the midplane is relatively smaller.

At Ra=10^5, a significant change of the flow configuration is observed, as it looks much more regular than in the previous cases. In fact a single vortex near the hot wall is observed. This is unexpected as it is usually observed that when the control parameters increase, the flow complexity also increases. The larger order in the flow configuration is accompanied by a much more regular distribution of the isotherms with respect to the previous cases: The temperature jumps are concentrated near the vertical walls, while the temperature is about constant in the bulk of the fluid. The counterintuitive behavior of the flow is also confirmed by the value of the three velocity components, reported in Table III: One might expect a monotonic increase of these values as Ra increases; on the contrary, the component u reaches the minimum value at Ra=10^5, v and w reach the minimum value at Ra=10^4.
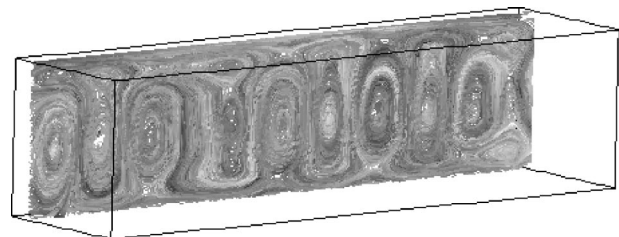
FIG. 9. Pr=23, Ra=4.3×10^8, and Ma=10 000—LIC representation at the plane $z=0.85$.

FIG. 10. $Pr=23$, $Ra=4.3\times10^8$, and $Ma=10\,000$—Isothermal lines at the plane $z=0.5$.

At $Ra=5\times10^6$, the flow structure no longer consists of a unique large roll but two new rolls superimposed to the initial structure appear: The first one appears in the lower region near the hot wall, the second one in the upper region near the cold wall. This change of the flow configuration does not affect the thermal field.

At $Ra=5\times10^7$, the flow configuration looks quite different with respect to the one obtained in the previous case, because the two rolls now have a larger dimension: The first one has invaded all the upper half of the domain, the second one occupies all the lower half of the domain with the exception of a small region near the cold wall.

B. Transition to chaos

The next simulations have been performed for increasing values of Ra, assuming the numerical solution obtained at $Ra=5\times10^7$ as basic flow. The list of the temporal regimes obtained is reported in Table IV. Table V reports the maximum values of the three velocity components, the average Nusselt number in the x direction and the temporal regime which characterizes each simulation, as a function of Ra. For the unsteady solutions, the quantities reported in the table have been averaged over a sufficiently long time interval.

At $Ra=4.25\times10^8$ an unsteady periodic flow with a fundamental frequency was found. A fast Fourier transform (FFT) applied on the time history of the x-component of velocity (u) at the point (0.8, 0.5, 0.4) highlights the presence of one fundamental frequency $f_1=1.4132$. Here we detected the first Hopf bifurcation.

Starting from the flow configuration obtained at $Ra=5\times10^7$, an increase in Ra at 4.3×10^8 leads to the second Hopf bifurcation with a transition to a quasi-periodic regime with two incommensurate frequencies. Figures 4 and 5 show respectively the transient history of the x-component of velocity (u) and of temperature at the point (0.8, 0.5, 0.4). A FFT applied on the time history of the x-component of velocity (u) (Fig. 6) identifies the value of the two main frequencies, $f_1=1.4038$ and $f_2=0.1953$, which coexist with several harmonics. Figures 7–9 show the LIC representations at

TABLE VI. Periodic and quasiperiodic regimes: Main frequencies and their ratio as a function of Ra.

Ra	f_1	f_2	f_1/f_2
4.25×10^8	1.4132	-	-
4.3×10^8	1.4038	0.1953	7.187
4.5×10^8	1.3916	0.1708	8.147
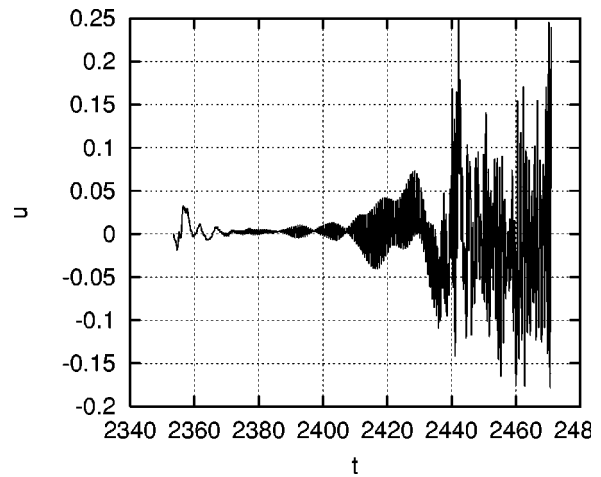
FIG. 11. $Pr=23$, $Ra=5\times10^8$, and $Ma=10\,000$—Time history of the x-component of velocity (u) at the point (0.8, 0.5, 0.4).

three different z-normal planes, respectively, $z=0.15$, $z=0.5$, and $z=0.85$. An analysis of the flow configuration shows that the one roll configuration is destroyed and replaced by a sequence of ten rolls, whose axes are parallel to the z axis. This is a configuration similar to those observed in other convection problems (e.g., the Rayleigh-Bénard convection) [19]. Figure 10 shows the isothermal lines in the z-normal plane at $z=0.5$. We can observe that the thermal field is not influenced by the change in the flow structure and that the destabilization is entirely hydrodynamical.

Starting from the flow configuration obtained at $Ra=5\times10^7$, the next simulation has been executed at $Ra=4.5\times10^8$. In this case the flow remains quasiperiodic even for this value of Ra, with slightly different values of the main frequencies. We observe that both the value of the main frequencies decrease, while their ratio increases as Ra grows (Table VI).

At $Ra=5\times10^8$, a transition to a chaotic regime is observed. However this is not a direct transition and the presence of a quasiperiodic regime with three incommensurate frequencies has been observed during the initial stage of this
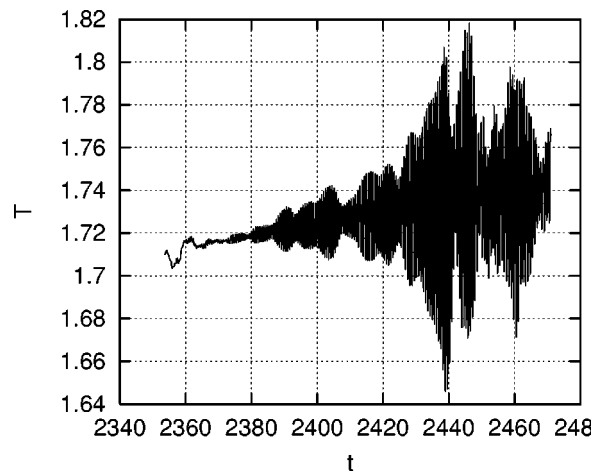
FIG. 12. $Pr=23$, $Ra=5\times10^8$, and $Ma=10\,000$—Time history of the temperature at the point (0.8, 0.5, 0.4).
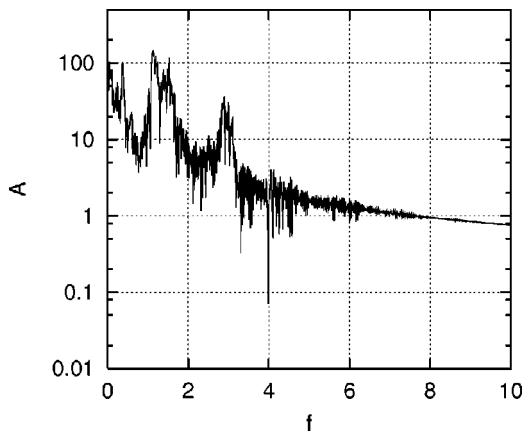
FIG. 13. Pr=23, Ra=5×10^8, and Ma=10 000—FFT executed on the time history of the x component of velocity (u) at the point (0.8, 0.5, 0.4).

simulation. Figures 11 and 12 show, respectively, the transient history of the x-component of velocity (u) and of temperature at the point (0.8, 0.5, 0.4). As shown in Fig. 13, the FFT of the time history of the x-component of velocity (u) highlights the presence of three fundamental frequencies ($f_1=4.88\times10^{-2}, f_2=0.378$, and $f_3=1.135$). However, a broadband noise, typical of the chaotic systems, is also observable.

In conclusion, the bifurcation sequence observed is the following:

$$S \rightarrow P \rightarrow QP_2(\rightarrow QP_3) \rightarrow N.$$

This is the well-known Ruelle-Takens route, which has been subject of theoretical as well as practical investigations in several different flow systems. We detected it numerically for the first time in the flow system presently studied.

We have studied the system up to reaching the maximum value of the bifurcation parameter Ra=10^9 and observed that the flow still keeps evolving towards chaos.

C. Persistence of the steady state

Further simulations have been performed following the scheme indicated in Table VII. Table VIII reports the maximum values of the three velocity components, the average Nusselt number in the x direction, and the kind of regime which characterizes each simulation, as a function of Ra. In Fig. 14 the flow evolution for the four selected values of Ra can be seen. In this figure, the LIC representations in the z-normal plane at $z=0.5$ are reported.

TABLE VII. Persistence of the steady state: List of temporal regimes obtained as a function of the increase in Ra.

From Ra		To Ra	Regime
5×10^7	$\rightarrow$	10^8	S
10^8	$\rightarrow$	3×10^8	S
3×10^8	$\rightarrow$	4×10^8	S
4×10^8	$\rightarrow$	4.3×10^8	S

TABLE VIII. Value of Ra, corresponding maximum values of velocity components, Nusselt number in the middle plane normal to the x axis and temporal regime.

Ra	u_{max}	v_{max}	w_{max}	Nu_x	Regime
10^8	0.134	8.798×10^{-2}	3.548×10^{-2}	59.182	S
3×10^8	0.192	0.123	5.554×10^{-2}	76.542	S
4×10^8	0.255	0.274	7.627×10^{-2}	96.444	S
4.3×10^8	0.263	0.291	7.880×10^{-2}	98.636	S

Starting the simulation from the flow configuration obtained at Ra=5×10^7, the next simulation has been performed at Ra=10^8, obtaining a steady flow configuration which looks similar to the initial one. From this numerical solution, the next simulation has been performed at Ra=3×10^8, obtaining again a steady flow configuration similar to the initial one.

Starting the simulation from the flow configuration obtained at Ra=3×10^8, the next case that we have run was at Ra=4×10^8; a significant difference emerged, that is the two rolls merged into a single large one and gave rise to a much more regular configuration, which looks like the Poiseuille-Couette flow between parallel planes.

Starting the simulation from the flow configuration obtained at Ra=4×10^8, further simulations have been performed at Ra=4.2×10^8 and 4.3×10^8: in both cases, steady configurations were obtained again. This is a significant result, as we have seen in the previous paragraph that at Ra=4.3×10^8 a quasiperiodic flow was also found. These flows differ also in the spatial configuration, actually the steady flow consists of one roll whereas the quasiperiodic one fea-
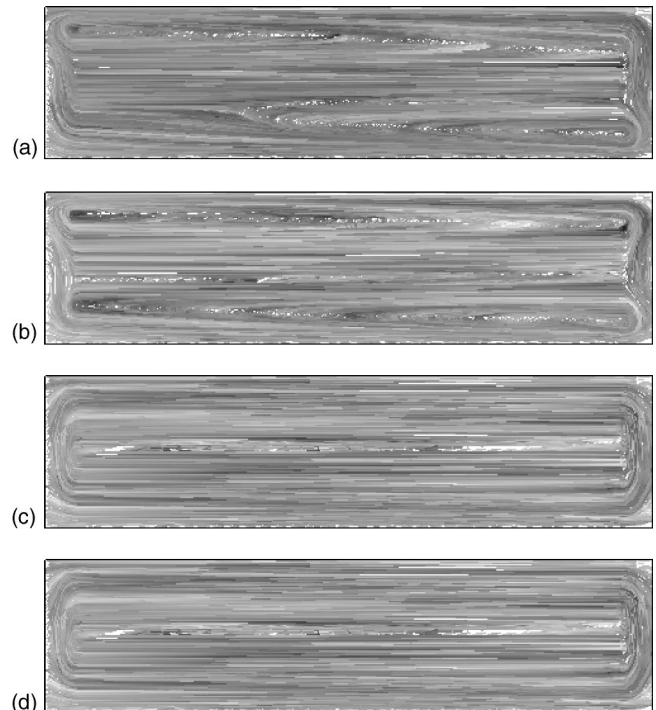
FIG. 14. Pr=23, Ma=10 000—LIC representation at the plane $z=0.5$ for Ra=10^8 (a), 3×10^8 (b), 4×10^8 (c), and 4.3×10^8 (d).

tures a ten roll structure. This aspect suggests that the numerical flows obtained depend on the thermal history of flow, that is, in particular, on the initial flow and temperature fields.

V. CONCLUSIONS

We have computed by numerical simulation the bifurcation pattern of the thermocapillary horizontal convection flow of SCN (Pr=23) in an open top parallelepipedic cavity with the dimension $(4 \times 1 \times 1)$. The bifurcation parameter is the Rayleigh number that was investigated in the range $[150; 5 \times 10^8]$; the Marangoni number was kept at Ma=10^4.

The simulation at Ra=150 was started from rest; the following simulations were obtained by stepping up the value of Ra and starting the computation from the flow and thermal field just obtained at the previous run. Following this procedure, several steady flow configurations have been obtained for Ra$\leq 5 \times 10^7$, characterized by the one roll, the two roll, and the ten roll flow structures respectively, for increasing values of Ra. Although the morphology of such flows is quite different, heat transport develops in similar ways, as can be deduced from the plots of the isothermal lines. Actually, all these cases exhibit sharp boundary layers at the boundaries at constant temperature and vertically stratified bulk. For Ra such that $5 \times 10^7 \leq$ Ra$< 5 \times 10^8$, we experienced two different strategies for the initialization of the time integration. First, by continuing with the procedure described above, we simply obtained the persistence of the steady regime with, respectively, two-roll and single-roll flow structures for increasing values of Ra. In the other case, by choosing as the initial condition the flow and thermal fields computed at the minimal extremum value Ra=5×10^7 we found the occurrence of periodic and quasiperiodic flows. At Ra=5×10^8, chaos arises through a transitory three-frequence quasiperiodic regime according to the Ruelle-Takens route. These differences highlight a strong dependence of the flows on their thermal history aspect that will be the subject of further investigation.

In principle, we cannot exclude that the system of partial differential equations that we solve, due to nonlinearity, admits other bifurcation patterns along Ra variations depending on different choices of the initial flow. In the same way, different preconditioners within the solution of the nonlinear discretized model might induce a jump from a branch to another in the bifurcation pattern of the flow. However, we stress that the ILU preconditioner used here is most robust and also the presented solutions have been computed up to the round-off error.

[1] D. Henry and M. Buffat, J. Fluid Mech. **374**, 145 (1998).

[2] D. T. J. Hurle, E. Jakeman, and C. P. Johnson, J. Fluid Mech. **64**, 565 (1974).

[3] D. Schwabe, A. Scharmann, F. Preisser, and R. Oeder, J. Cryst. Growth **43**, 305 (1978).

[4] M. Smith and S. Davis, J. Fluid Mech. **132**, 119 (1983).

[5] R. J. Riley and G. P. Neitzel, J. Fluid Mech. **359**, 143 (1998).

[6] D. Villers and J. K. Platten, J. Fluid Mech. **234**, 487 (1992).

[7] M. Smith, Phys. Fluids **29**(10), 3182 (1986).

[8] H. Ben Hadid and B. Roux, J. Fluid Mech. **235**, 1 (1992).

[9] M. G. Braunsfurth and G. M. Homsy, Phys. Fluids **9**(5), 1277 (1997).

[10] P. Bergé, Y. Pomeau, and C. Vidal, *Order Within Chaos—Towards a Deterministic Approach to Turbulence* (Wiley, New York, 1984).

[11] J. P. Gollub and S. V. Benson, J. Fluid Mech. **100**, 449 (1980).

[12] A. M. Guzman and C. H. Amon, J. Fluid Mech. **321**, 25(1996).

[13] E. Bucchignani and F. Stella, Numer. Heat Transfer, Part A **36**, 17 (1999).

[14] E. Bucchignani and D. Mansutti, Int. J. Numer. Methods Heat Fluid Flow **10**(2), 179 (2000).

[15] F. Harlow and J. Welch, Phys. Fluids **8**, 21 (1965).

[16] F. Stella and E. Bucchignani, Numer. Heat Transfer, Part B **30**, 315 (1996).

[17] H. Van der Vorst, SIAM (Soc. Ind. Appl. Math.) J. Sci. Stat. Comput. **13**(2), 631 (1992).

[18] B. Sikorski and P. Leoncini, Eighth International Symposium on Flow Visualization, Sorrento, Italy, 1998, edited by G. M. Carlomagno and I. Grant (unpublished).

[19] F. Stella and E. Bucchignani, Numer. Heat Transfer, Part A **36**, 1 (1999).